J. Fluid Mech. (2023), *vol*. 971, A35, doi:10.1017/jfm.2023.688

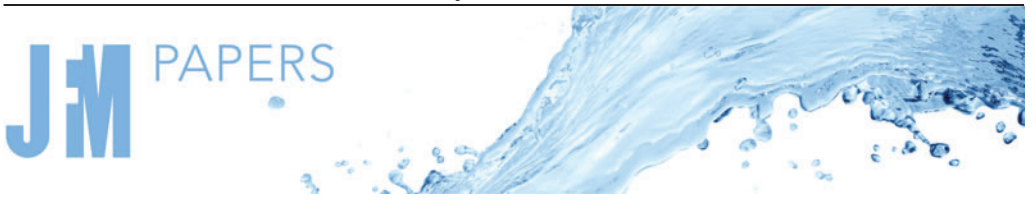

Nonlinear surface Ekman effects on cyclonic and anticyclonic vortices

L. Zavala Sansón[1],†, **I.M. García-Martínez**[1] **and J. Sheinbaum**[1]

[1]Department of Physical Oceanography, CICESE, Ensenada, Baja California 22860, Mexico

(Received 24 December 2022; revised 15 July 2023; accepted 10 August 2023)

The transfer of momentum between the atmosphere and oceanic motions affected by the Earth's rotation occurs through the thin surface Ekman layer. The exchange depends on the surface wind stress, which produces the Ekman pumping of fluid to the ocean upper layer. The Ekman pumping mainly depends on: (i) the curl of the wind stress and (ii) the advection of vorticity due to the Ekman transport. The wind stress is usually parametrised as a quadratic function of the relative speed between the wind and the ocean currents, providing a feedback mechanism between the two fluids. Under steady and spatially uniform wind conditions over mesoscale vortices, the first mechanism generates vertical motions that induce the vortex decay (top drag), while the second promotes the horizontal advection of vorticity in the Ekman transport direction. This study examines the nonlinear effects of both mechanisms in cyclonic and anticyclonic vortices. The analyses consist of simple analytical approximations and nonlinear numerical simulations of quasi-two-dimensional vortices. When considering only the top drag mechanism, it is found that anticyclones decay faster than cyclones. By considering only the vorticity-advection effect, the vortices acquire horizontal momentum and drift; furthermore, anticyclones are reinforced while cyclones are weakened. The joint action of both mechanisms and the possible consequences on vertical transport properties are also discussed.

Key words: ocean processes, quasi-geostrophic flows, vortex dynamics

1. Introduction

In the wide range of oceanic motions, mesoscale vortices play a fundamental role because they concentrate an important fraction of the global surface kinetic energy (Klein *et al.* 2019). With typical radii of the order of $O(10–100)$ km, nonlinear mesoscale eddies usually travel distances much further than their size and remain active from weeks to months or even years. Along their trajectory, these vortices can transport and mix different physical,

† Email address for correspondence: lzavala@cicese.mx

chemical and biological properties around the ocean (Chelton, Schlax & Samelson 2011). An essential characteristic of mesoscale vortex motions is that they are strongly influenced by the Earth's rotation, and consequently, their horizontal motions are at least an order of magnitude greater than vertical displacements. Nevertheless, vertical motions are of primary relevance for material exchange of nutrients, carbon, heat and momentum between the upper surface and interior layers (McGillicuddy 2016).

The vertical velocity in the ocean may be associated with several mechanisms: free surface effects, horizontal divergence, tilting of fluid columns, topography effects, baroclinic processes, and horizontal and vertical mixing, among others. Here we investigate the vertical velocity due to the surface wind stress on mesoscale vortices. The influence of the lower atmosphere on the ocean takes place through the surface boundary layer (the Ekman layer), which is usually thin (of the order of tens of m) with respect to the average vortex depth in the mixed layer (a few hundred m). The flow inside the Ekman layer is generally divergent; therefore, it injects or extracts fluid from the balanced flow underneath. The resulting vertical velocity is usually called Ekman pumping or suction, and sometimes just the Ekman condition (Pedlosky 1987). Despite the weak values of the Ekman condition (from the order of 10^{-1} to a few $\mathrm{m\,day^{-1}}$), the resulting upward and downward anomalies of the density field either reinforce or weaken the strength of mesoscale structures, in addition to having a significant influence on transport properties.

The Ekman pumping depends on the wind stress over the ocean's free surface. A suitable expression for the Ekman vertical velocity was derived by Stern (1965) as

$$w_s = \frac{1}{\rho_0}\nabla \times \left(\frac{\boldsymbol{\tau}}{f+\omega}\right), \tag{1.1}$$

where $\boldsymbol{\tau} = (\tau^x, \tau^y)$ is the two-dimensional stress vector with components in the horizontal directions (x, y), f the Coriolis parameter and ω the vertical component of the relative vorticity. This expression can be decomposed as $w_s = w_d + w_a$, where

$$w_d = \frac{1}{\rho_0(f+\omega)}\nabla \times \boldsymbol{\tau}, \tag{1.2}$$

$$w_a = \frac{1}{\rho_0(f+\omega)^2}\left(\tau^x\frac{\partial \omega}{\partial y} - \tau^y\frac{\partial \omega}{\partial x}\right). \tag{1.3}$$

The first part, w_d, is given by the wind stress curl, $\nabla \times \boldsymbol{\tau}$. The second contribution, w_a, depends on the advection of vorticity by the Ekman transport, $\boldsymbol{\tau}^\perp \cdot \nabla\omega$, where $\boldsymbol{\tau}^\perp = (-\tau^y, \tau^x)$. On a β-plane, there is an additional pumping term associated with the latitudinal change of the Coriolis parameter; such a contribution is proportional to the zonal stress τ^x and is approximately two orders of magnitude smaller than the other contributions (Gaube *et al.* 2015), even for strong zonal winds, so it has been neglected.

A key point to study the effects of w_d and w_a on geostrophic flows is the choice of the wind stress parametrisation. The classical wind-stress bulk formula is based on a quadratic function of the wind velocity $\boldsymbol{U}$ as $\boldsymbol{\tau} = \rho_a C_D|\boldsymbol{U}|\boldsymbol{U}$, where ρ_a is the air density and C_D a drag coefficient (Hellerman 1967). A more suitable parametrisation considers that the air–sea momentum transfer depends on the relative velocity between the wind and the ocean current $\boldsymbol{u}$, so the bulk formula is (Dewar & Flierl 1987; Pacanowski 1987)

$$\boldsymbol{\tau} = \rho_a C_D|\boldsymbol{U} - \boldsymbol{u}|(\boldsymbol{U} - \boldsymbol{u}). \tag{1.4}$$

When using this expression, the resulting vertical velocity has been identified as a current-induced Ekman pumping (Gaube *et al.* 2015). In this case, the Ekman condition

generates a feedback mechanism or current-induced surface stress (Renault *et al.* 2016) because the oceanic flow influences the wind stress.

Several studies have addressed the effects of w_d and/or w_a on ocean motions using parametrisation (1.4). Although the energy transfer is mostly from the atmosphere to the ocean, the wind stress dependence on the relative velocity allows the loss of energy from the ocean to the atmosphere, as suggested by observations (Xu, Zhai & Shang 2016) and numerical simulations (Renault *et al.* 2016). The wind damping effects have been demonstrated for spatially uniform background wind, a reasonable approach for scales shorter than 260 km, according to the recent estimations of Rai *et al.* (2021). Under uniform wind conditions, Dewar & Flierl (1987) considered the decay of mesoscale rings due to w_d. Their results showed that the predominant vertical motion is concentrated at the vortex core and has the opposite sign to that of the peak vorticity. This configuration triggers a damping effect or 'top drag' in oceanic rings: upwelling in the interior of anticyclones and downwelling in the core of cyclones. On the other hand, the vorticity-advection effect given by w_a for uniform wind conditions consists of an upwelling and downwelling dipolar structure oriented in the wind direction (McGillicuddy, Ledwell & Anderson 2008). Since the net vertical motion is too small (but not null), this term has received less attention or has been ignored.

Other works have discussed the Ekman contributions in the vertical transport properties within oceanic vortices. McGillicuddy *et al.* (2007) concluded that the predominant upwelling of nutrients in anticyclones is due to w_d because it is localised at the core of the vortex, while the dipolar form of w_a nearly cancels out upward and downward motions (McGillicuddy *et al.* 2008). Mahadevan, Thomas & Tandon (2008), in contrast, argued that upwelling should occur at the rim of the vortex, caused either by w_a or submesoscale processes. More recently, Gaube *et al.* (2015) pointed out that both contributions to the vertical velocity are comparable in magnitude under typical wind conditions and gave a detailed description of their spatial structures in the world's oceans. Estrada-Allis *et al.* (2019) performed numerical simulations under realistic conditions to study the vertical velocity dynamics within an anticyclone. Chen, Gaube & Pallàs-Sanz (2020) compared the output of baroclinic simulations using either the wind or the wind–sea relative velocity to calculate the surface stress and examined the role of several types of vertical fluxes to evaluate the nutrient budget in the euphotic zone. Following a similar numerical approach, Wilder *et al.* (2022) studied Ekman effects on the stability of idealised anticyclones. For uniform wind stress conditions and without considering the ocean-atmosphere relative velocity (1.4), Wenegrat & Thomas (2017) studied the structure of the Ekman transport associated with the flow curvature and obtained analytical solutions for circular vortices.

In this paper, we discuss the effects of the Ekman vertical velocities w_d and w_a on cyclones and anticyclones. It is shown that the vortex decay associated with w_d is faster for anticyclones than cyclones. In contrast, the vorticity-advection contribution w_a reinforces anticyclones and weakens cyclones; furthermore, this effect produces the drift of both types of vortices at a right angle of the wind direction, as first predicted by Stern (1965). To better understand these effects, we use an idealised one-layer model to derive the vortex decay, and the cyclone/anticyclone drift analytically. It is shown that, although the latter effect is rather modest, it is able to modify the vortex trajectory in β-plane simulations.

Differences of Ekman effects in cyclones and anticyclones may be relevant under strong and persistent wind conditions. From an oceanographic point of view, our study is motivated by the occurrence of intense northerly wind events during winter in the Gulf of Mexico, the so-called 'Nortes', which reach speeds of more than $20\,\mathrm{m\,s^{-1}}$ and may last 2–6 days (Romero Centeno & Zavala Hidalgo 2021). The Nortes may interact

with large anticyclonic eddies shed by the Loop Current that travel westwards through the basin during several months (e.g. Tenreiro *et al.* 2018; Meunier *et al.* 2020). In some cases, these warm vortices develop enhanced surface chlorophyll concentrations, presumably due to vertical fluxes driven by eddy–wind interactions (Damien *et al.* 2021). Another motivation is found in the Caribbean Sea, where the easterly winds intensify and form the Caribbean low-level jet (Amador 2008). The jet speed is 6–8 m s^{-1} at the sea surface (and up to 15 m s^{-1} at 925 hPa), with maxima during summer and winter, when the intense wind conditions can last for several weeks (García-Martínez & Bollasina 2020). The low-level jet may affect cyclonic and anticyclonic eddies that have important contributions to the dynamics of the Caribbean Sea circulation (Jouanno *et al.* 2012). Strong cyclone-anticyclone asymmetries have also been documented in other oceanic regions (Mkhinini *et al.* 2014).

From the fluid dynamics point of view, our calculations are related to former analyses of nonlinear bottom Ekman effects in rotating tank experiments, either with a flat bottom (Zavala Sansón & van Heijst 2000) or variable topography (Zavala Sansón & van Heijst 2002). For a flat bottom, it is found that cyclones decay faster than anticyclones (Zavala Sansón 2001; Zavala Sansón, van Heijst & Backx 2001), opposite to the Ekman surface effect that we will discuss here. The difference between cyclones and anticyclones is a relevant issue for ocean turbulence because it may help to explain asymmetries in global or regional vorticity distributions, stability properties (Mahdinia *et al.* 2017), and to better understand cascade processes in turbulent regimes (Ding *et al.* 2020) or the global distribution of turbulent shear that generates ocean mixing due to mesoscale eddies (Zhang *et al.* 2018).

The paper is organised as follows. Section 2 presents the nonlinear Ekman effects in the dynamical model, together with analytical results concerning the decay and drift of cyclones and anticyclones. Section 3 is devoted to numerical simulations that show the evolution of vortices and evaluate the calculations from the previous section. In § 4, the results are summarised and discussed.

2. Surface Ekman effects on cyclones and anticyclones

We consider a fluid layer with density ρ_0 and constant thickness H at the upper ocean under the influence of the Earth's rotation and the surface wind stress vector $\boldsymbol{\tau}$. Rotation effects restrict motions to be predominantly horizontal, so we consider a planar system with coordinates (x, y). For the β-plane approximation, the Coriolis parameter is $f = f_0 + \beta y$, with f_0 its value at a mid-latitude and β its latitudinal gradient. The flow is described by the horizontal velocity vector $\boldsymbol{u} = (u, v)$ and the vertical component of the relative vorticity $\omega = \partial_x v - \partial_y u$. The flow is relatively slow for mesoscale motions with a dynamical Rossby number $\omega_{max}/f_0 < 1$, which is a few times larger than the standard Rossby number $U_o/f_0 L$ based on the characteristic length and velocity scales (Stegner & Dritschel 2000). The vertically integrated vorticity equation for a flat bottom and a rigid-lid is

$$\frac{\partial \omega}{\partial t} + \boldsymbol{u} \cdot \nabla \omega + \beta v = \frac{f_0}{H} w, \tag{2.1}$$

where the weak Ekman pumping w at the right-hand side appears as the surface boundary condition (Vallis (2017), Chap. 14). The simplified form of the forcing term is associated with the smallness of the vertical velocity, as discussed in Appendix A.

For w, we consider either the full Stern's expression (1.1) or any of its main components w_d (1.2) or w_a (1.3). In all cases, the wind stress is based on the air-sea relative velocity (1.4) with a spatially uniform wind field $\boldsymbol{U}$. It is assumed that the wind speed is much more

intense than the ocean currents, $|\boldsymbol{U}| >> |\boldsymbol{u}|$. In the rest of this section, we present some theoretical analyses concerning the effects of w_d and w_a in cyclones and anticyclones, and in § 3, we study the Ekman effects in nonlinear numerical simulations.

2.1. *Spatial structure of w_d and w_a*

Here we revisit the spatial structure of the pumping terms in the presence of a uniform wind to better understand their influence on cyclones and anticyclones. The surface stress $\boldsymbol{\tau}$ (1.4) and its curl are calculated using a uniform large-scale northerly wind

$$\boldsymbol{U} = (0, -V_w), \quad |\boldsymbol{U}| \equiv V_w. \tag{2.2a,b}$$

The vortex model is an isolated circular flow whose vorticity and azimuthal velocity profiles in polar coordinates are given by

$$\omega(r) = \omega_0 \left[1 - \frac{\alpha}{2}\left(\frac{r}{R}\right)^{\alpha}\right] \exp\left[-\left(\frac{r}{R}\right)^{\alpha}\right], \tag{2.3}$$

$$v(r) = \frac{\omega_0 r}{2} \exp\left[-\left(\frac{r}{R}\right)^{\alpha}\right], \tag{2.4}$$

where ω_0 is the peak vorticity, R a horizontal length scale, r the radial distance to the centre of the vortex and α a shape parameter that determines the steepness of the profiles (Carton & McWilliams 1989). The structure is isolated because it has zero total circulation: the cyclonic or anticyclonic core is surrounded by an annulus of opposite-sign vorticity. This vortex is often used to model experimental vortices in the laboratory (Kloosterziel & van Heijst 1992; van Heijst & Clercx 2009; Zavala Sansón & van Heijst 2014), and similar structures are also helpful for representing mesoscale oceanic vortices (e.g. Gaube *et al.* 2015).

Figure 1 shows the spatial structure of w_d and w_a for three magnitudes of a uniform northerly wind (average, moderately intense and strong) for an intense anticyclonic vortex. The current-induced Ekman pumping (figure 1*a–c*) has a dominant pattern with an opposite sign of the vortex core (upwelling). In contrast, the vorticity-advection vertical velocity (figure 1*d–f*) has a dipolar structure with upwelling (downwelling) to the right (left)-hand side of the wind. In both cases, the lower intensity regions surrounding the vortex are of secondary importance and are associated with the chosen vortex model.

To better appreciate the magnitude and distribution of the vertical velocities, figure 2 presents the profiles $w_d(x, 0)$ and $w_a(x, 0)$ for cyclones and anticyclones subject to different wind strength. The following are observed.

(i) The Ekman velocities in all cases are enhanced for stronger winds. For instance, the current-induced velocity within the anticyclone in figure 2(*a*) goes from less than $1\,\mathrm{m\,d^{-1}}$ for $V_w = 7.5\,\mathrm{m\,s^{-1}}$ to nearly $3\,\mathrm{m\,d^{-1}}$ for the intense wind $V_w = 22.5\,\mathrm{m\,s^{-1}}$. The upwelling and downwelling generated by the vorticity-advection term are even larger: approximately 6 and $-6\,\mathrm{m\,d^{-1}}$, respectively, see figure 2(*c*).

(ii) As expected, the profiles are mirror-shaped for cyclones and anticyclones, but the absolute magnitudes are not the same. The positive w_d velocity in the anticyclone is stronger than the negative velocity in the cyclone (figure 2*a*,*b*). This difference is an indication that anticyclones decay faster than cyclones.

(iii) Regarding the magnitude of w_a, note that the downward velocity is larger than the upward velocity in both anticyclones (figure 2*c*) and cyclones (figure 2*d*). The asymmetry is caused by the relative wind stress, which is enhanced when the northerly wind and the current flow are in opposite directions.

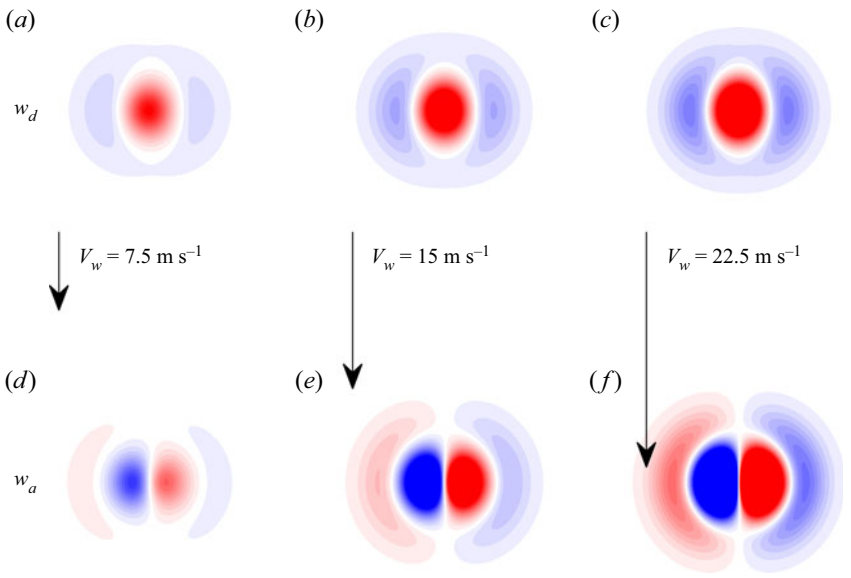

Figure 1. Spatial structure of the pumping terms (*a–c*) w_d and (*d–f*) w_a generated by a uniform northerly wind (2.2*a*,*b*) with three different magnitudes V_w and blowing over an anticyclonic vortex with vorticity profile (2.3). Red (blue) colours indicate upwelling (downwelling). The vortex parameters are $R = 100$ km, $\omega_0/f_0 = -0.25$, $\alpha = 2$. The vortex is centred at the origin of the coordinate system.

(iv) Both the upwelling and downwelling w_a velocities are more significant in the anticyclone than in the cyclone (compare figures 2*c* and 2*d*).

The pumping fields lift up or push down water through the mixed layer, but the fluid parcels or any passive tracer is also subject to the swirling flow around the vortex core. Thus, an appropriate way to evaluate the net vertical velocity is by taking azimuthal averages (McGillicuddy *et al.* 2008). Using the azimuthal coordinate θ, we calculate such averages as

$$\left.\begin{aligned} \bar{w}_d(r) &= \int_0^{2\pi} w_d \,\mathrm{d}\theta, \\ \bar{w}_a(r) &= \int_0^{2\pi} w_a \,\mathrm{d}\theta. \end{aligned}\right\} \tag{2.5}$$

Figure 3(*a*,*b*) shows the radial profiles of the azimuthally averaged w_d pumping terms. The velocity scale is kept the same as in figure 2(*a*,*b*), so we can appreciate that the integrated magnitude of the pumping terms at the vortex centre is similar to that found in the zonal profiles. In contrast, the integrated w_a profiles are strongly reduced, as shown in figure 3(*c*,*d*), because the upwelling side is nearly cancelled out by the downwelling region in both vortices. However, the residual pumping is not zero but slightly negative and off the vortex centre for cyclones and anticyclones. This net downward flow suggests that $\bar{w}_a$ produces a weak damping effect on the cyclone and slightly intensifies the anticyclone, as we shall verify below.

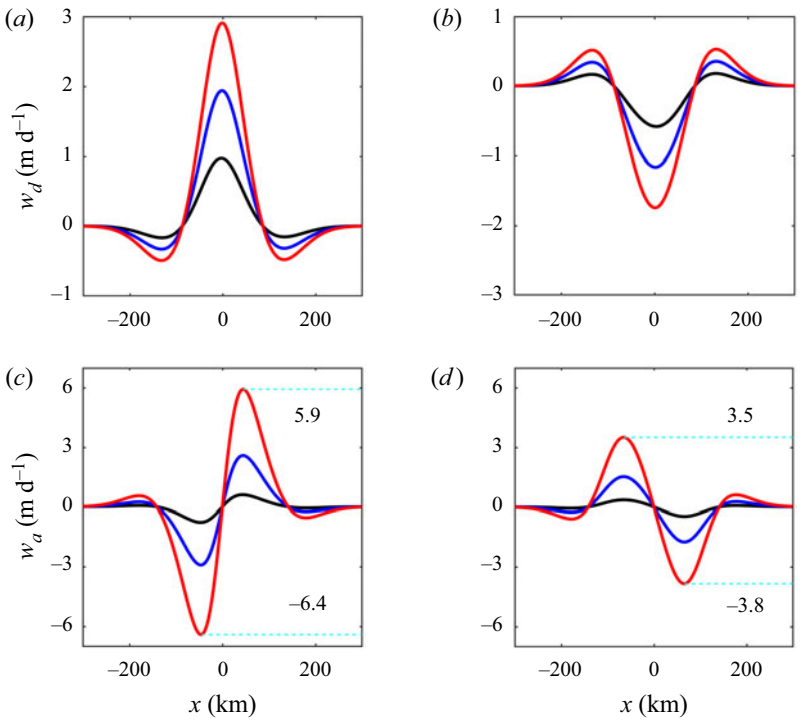

Figure 2. Profiles along the x-direction of the pumping terms w_d and w_a for (a,c) anticyclones and (b,d) cyclones. The colours indicate the wind magnitude: $V_w = 7.5\,\mathrm{m\,s^{-1}}$ (black), $V_w = 15\,\mathrm{m\,s^{-1}}$ (blue), $V_w = 22.5\,\mathrm{m\,s^{-1}}$ (red). Vortex parameters as in figure 1.

2.2. *Effects of w_d: vortex decay*

Let us now examine the nonlinear decay of circular vortices due to the Ekman pumping term w_d. The change of relative vorticity on the f-plane is approximated as

$$\frac{\partial \omega}{\partial t} = \frac{f_0}{H} w_d. \tag{2.6}$$

Using $\omega < f_0$, the Ekman pumping is expanded in Taylor series as

$$w_d = \frac{1}{\rho_0 (f_0 + \omega)} \nabla \times \boldsymbol{\tau} \approx \frac{1}{\rho_0 f_0} \left(1 - \frac{\omega}{f_0}\right) \nabla \times \boldsymbol{\tau}. \tag{2.7}$$

Without loss of generality, we concentrate on the large-scale northerly wind (2.2a,b). Then, the surface stress $\boldsymbol{\tau}$ (1.4) can be simplified by using the fact that the wind speed is much faster than the ocean currents, $u, v << V_w$. After some algebra to simplify the product $|\boldsymbol{U} - \boldsymbol{u}|(\boldsymbol{U} - \boldsymbol{u})$, the stress is approximated as

$$\boldsymbol{\tau} = \rho_a C_D V_w (-u, -V_w - 2v). \tag{2.8}$$

The curl is

$$\nabla \times \boldsymbol{\tau} = \rho_a C_D V_w \left(-2\frac{\partial v}{\partial x} + \frac{\partial u}{\partial y}\right). \tag{2.9}$$

An equivalent expression for $\nabla \times \boldsymbol{\tau}$ was found by Dewar & Flierl (1987). Assuming that the vortex remains circular, then $\partial v/\partial x = -\partial u/\partial y$ at the centre, so the stress curl at the

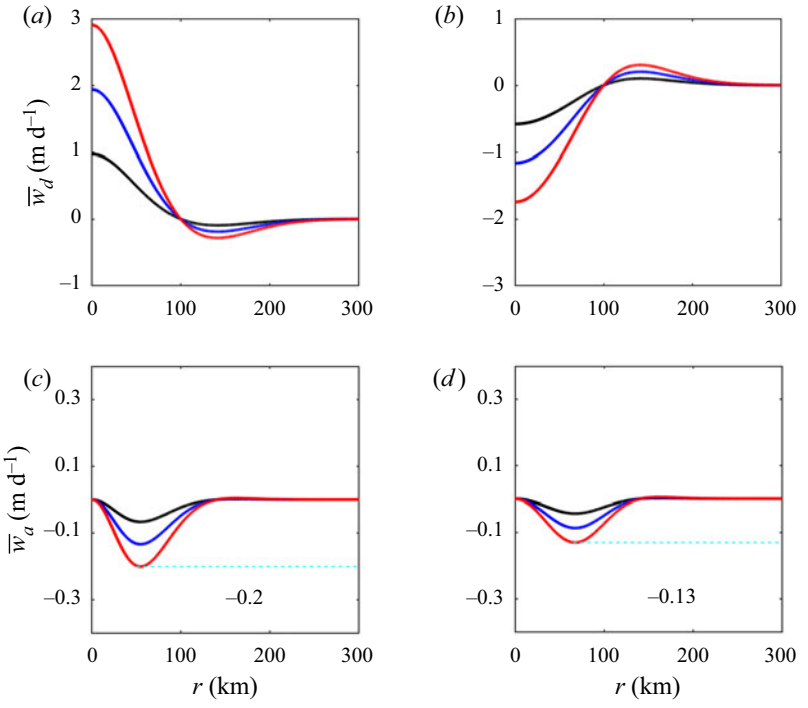

Figure 3. Radial profiles of the azimuthally averaged pumping terms w_d and w_a for (a,c) anticyclones and (b,d) cyclones. The colours and vortex parameters are as in figure 2.

origin can be written as

$$(\nabla \times \boldsymbol{\tau})_c = -\tfrac{3}{2}\rho_a C_D V_w \omega_c, \tag{2.10}$$

where ω_c is the peak vorticity. Plugging (2.10) in (2.7) yields

$$w_d = -\frac{3}{2}\frac{\rho_a C_D V_w}{\rho_0 f_0}\left(1 - \frac{\omega_c}{f_0}\right)\omega_c. \tag{2.11}$$

Substituting in (2.6) gives an equation for the peak vorticity decay:

$$\frac{\mathrm{d}\omega_c}{\mathrm{d}t} = -\frac{3}{2}\frac{\rho_a C_D V_w}{\rho_0 H}\left(1 - \frac{\omega_c}{f_0}\right)\omega_c \equiv -\frac{1}{T f_0}(f_0 - \omega_c)\omega_c, \tag{2.12}$$

where the time scale T is defined as

$$T = \frac{2}{3}\frac{\rho_0 H}{\rho_a C_D V_w}. \tag{2.13}$$

The solutions of (2.12) are of the form

$$\omega_c(t) = \frac{\omega_0 \exp(-t/T)}{1 - (\omega_0/f_0)(1 - \exp(-t/T))}, \tag{2.14}$$

where ω_0 is the peak vorticity at $t = 0$. These are decaying solutions at the characteristic time T. The most important feature is that (2.14) distinguishes the vortex polarity in the denominator, implying that anticyclones ($\omega_0 < 0$) decay faster than cyclones ($\omega_0 > 0$). The solutions can be called nonlinear because of the form of the evolution equation (2.12).

Solutions (2.14) are equivalent – but not the same – to those applied for representing the decay of vortices due to bottom Ekman friction in rotating tank experiments (Zavala Sansón & van Heijst 2000). The comparison of top and bottom friction effects is further discussed in the last section.

The more conventional (exponential) decay is recovered in the limit of weak vortices $\omega/f_0 << 1$. In that case, the vertical velocity simplifies as

$$w_{lin} = \frac{1}{\rho_0 f_0} \nabla \times \boldsymbol{\tau}. \tag{2.15}$$

Thus, the vorticity equation (2.6) becomes linear:

$$\frac{\mathrm{d}\omega_c}{\mathrm{d}t} = -\frac{3}{2}\frac{\rho_a C_D V_w}{\rho_0 H}\omega_c \equiv -\frac{1}{T}\omega_c, \tag{2.16}$$

with exponentially decaying solutions

$$\omega_c(t) = \omega_0 \exp(-t/T). \tag{2.17}$$

In this approach, cyclones and anticyclones decay at the same rate. The linear decay was discussed by Gaube *et al.* (2015), who found the same eddy attenuation time scale T but followed a different approach. They considered a randomly directed wind $\boldsymbol{U} = V_w(\cos\theta, \sin\theta) >> \boldsymbol{u}$, and then averaged over a uniform θ-distribution to obtain a mean surface stress $\bar{\boldsymbol{\tau}}$ proportional to the surface currents. Using the curl $\nabla \times \bar{\boldsymbol{\tau}}$ in the linear Ekman condition (2.15) yields the same stress curl (2.9) and therefore the exponential decay (2.17) (see also Renault *et al.* 2016).

2.3. *Effects of w_a: vortex drift*

From the azimuthally averaged profiles in figure 3(*c*,*d*), we observed that $\bar{w}_a < 0$, so this downward velocity slightly intensifies anticyclones and weakens cyclones. However, the effect is relatively weak because the net pumping is small, as we shall corroborate in numerical simulations.

Another effect associated with w_a is the vortex translation in the direction of the Ekman transport, a process correctly predicted by Stern (1965) and, to the best of our knowledge, not discussed in previous studies. From Ekman theory, and ignoring the contribution of a solenoidal vector field (Wenegrat & Thomas 2017), the transport components are

$$\left.\begin{aligned} HU_E &= \frac{\tau^y}{\rho_0(f_0+\omega)}, \\ HV_E &= -\frac{\tau^x}{\rho_0(f_0+\omega)}, \end{aligned}\right\} \tag{2.18}$$

where (U_E, V_E) is the integrated velocity in the Ekman layer that the vortex eventually acquires. Since the northerly wind is such that $V_w >> v$, the only relevant stress component from (2.8) is $\tau^y \approx -\rho_a C_D V_w^2$, which implies that the vortex drifts westward with speed U_E. Assuming small ω/f_0 again, we approximate the speed using the peak

vorticity:

$$U_E \approx \frac{\tau^y}{\rho_0 H f_0^2}(f_0 - \omega_c),$$
$$= -\frac{\rho_a C_D V_w^2}{\rho_0 H f_0^2}(f_0 - \omega_c) \equiv -\frac{2}{3}\frac{V_w}{f_0 T}\left(1 - \frac{\omega_c}{f_0}\right), \tag{2.19}$$

where we introduced the characteristic time T defined in (2.13). Note that anticyclones move faster than cyclones due to factor $1 - \omega_c/f_0$. The vortex speed is approximately constant because ω_c does not change much under the influence of w_a (as we shall see later). Thus, the vortex displacement after time T_a is

$$\Delta x = -\frac{2}{3}\frac{V_w T_a}{f_0 T}\left(1 - \frac{\omega_c}{f_0}\right). \tag{2.20}$$

A conventional (or linear) displacement that would not distinguish between cyclones and anticyclones is obtained by assuming $\omega_c << f_0$, which yields

$$\Delta x_{lin} = -\frac{2}{3}\frac{V_w T_a}{f_0 T}. \tag{2.21}$$

2.4. *Relative importance of w_d and w_a*

There has been some discussion on the relative importance of w_d and w_a for typical oceanic vortices due to their differences in magnitude and spatial structure (McGillicuddy *et al.* 2007; Mahadevan *et al.* 2008). Here we propose an alternative view based on our previous results in § 2.2. The relative magnitude of the pumping terms is estimated as

$$\left|\frac{w_a}{w_d}\right| \approx \left|\frac{-\tau^y \partial\omega/\partial x}{(f_0+\omega)\boldsymbol{\nabla}\times\boldsymbol{\tau}}\right| \approx \left|\frac{(\rho_a C_D V_w^2) \quad (\omega_0/R)}{(f_0+\omega_0) \quad (-3/2)\rho_a C_D V_w \omega_0}\right|$$
$$= \frac{2/3}{(1+Ro)}\frac{|V_w|}{f_0 R}, \tag{2.22}$$

where we considered $\tau^y \approx -\rho_a C_D V_w^2$ from (2.8), the wind stress curl $\boldsymbol{\nabla}\times\boldsymbol{\tau}$ from (2.10), $f \approx f_0$ and the dynamical Rossby number $Ro = \omega_0/f_0$. Note that the denominator depends on the vortex sign contained in Ro, so it is verified that

$$\left|\frac{w_a}{w_d}\right|_{cyclones} < \left|\frac{w_a}{w_d}\right|_{anticyclones}. \tag{2.23}$$

This fact can be observed in figure 4(*a*), which presents the $|w_a/w_d|$ versus Ro curves for the three wind regimes. For the average wind, the current-induced velocity w_d dominates (black curve). For the moderately intense forcing, $|w_a/w_d| > 1$ for anticyclones and < 1 for cyclones (blue curve). The vorticity-advection velocity w_a is dominant in the strong wind regime (red line).

The previous estimate (2.22) only considers the characteristic magnitude of the pumping terms but not their spatial structure. A different comparison consists of using the azimuthally integrated pumping components. For the current-induced velocity $\bar{w}_d$, we can use again $\boldsymbol{\nabla}\times\boldsymbol{\tau}$ from (2.10) because the integrated pumping is approximately the same with or without integration (see the peak values in figures 2*a*,*b* and 3*a*,*b*). For $\bar{w}_a$, we have to consider that the upwelling at a flank of the vortex cancels most of the downwelling at

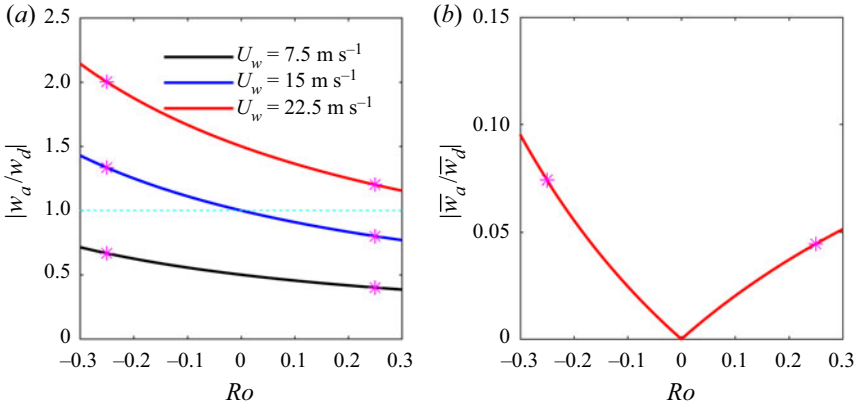

Figure 4. Ratio of the pumping terms as a function of the dynamical Rossby number. (*a*) Ratio based on the peak values of w_a and w_d estimated by (2.22) for three wind speeds. (*b*) Ratio of the azimuthally integrated pumping terms (2.24). This ratio does not depend on the wind speed. The stars in both panels indicate the anticyclonic and cyclonic cases in figures 2 and 3.

the other side, and the remaining part is the negative velocity found in figure 3(*c*,*d*). Thus, using (2.8), we estimate $\bar{w}_a \propto \tau^y \partial\omega/\partial x \approx (-\rho_a C_D V_w 2v)(\omega_0/R)$. The vortex azimuthal velocity is well approximated by its value at $R/2$, where the negative pumping takes place, so $v \approx \omega_0 R/6$ (to check for the factor 1/6, evaluate, for instance, the azimuthal velocity (2.4) at $r = R/2$). Thus,

$$\left|\frac{\bar{w}_a}{\bar{w}_d}\right| \approx \left|\frac{\overline{-\tau^y \partial\omega/\partial x}}{(f_0+\omega)\nabla\times\boldsymbol{\tau}}\right| \approx \left|\frac{(\rho_a C_D V_w \omega_0 R/3) \quad (\omega_0/R)}{(f_0+\omega_0) \quad (-3/2)\rho_a C_D V_w \omega_0}\right| = \frac{2/9}{(1+Ro)}|Ro|. \tag{2.24}$$

Now the comparison of the Ekman terms does not depend on the wind magnitude as its effect was cancelled out when estimating $\bar{w}_a$. Figure 4(*b*) shows the resulting curve, which reveals that the top drag velocity dominates, $|\bar{w}_a/\bar{w}_d| < 1$, for any (small) Rossby number.

3. Numerical simulations of circular vortices

The experiments in this section verify the previous results regarding the relative importance of the Ekman pumping terms w_d and w_a for circular vortices under the effect of a uniform wind. In most of simulations, we consider an f-plane but we also analyse further aspects of the nonlinear evolution of cyclones and anticyclones on the β-plane.

3.1. *Dynamical model and description of experiments*

We consider a two-dimensional (2-D) homogeneous flow governed by the vorticity equation (2.1). The vorticity-stream function formulation of this model is

$$\frac{\partial\omega}{\partial t} + J(\omega+\beta y, \psi) = \frac{f_0}{H}w, \tag{2.1}$$

where $J(a,b) = \partial_x a \partial_y b - \partial_y a \partial_x b$ is the Jacobian operator, H a depth scale and w the surface Ekman pumping. The horizontal velocity components are defined from the stream

Parameter	Symbol and value in arbitrary units
Domain size	$L = 1200\,\text{km}$
Depth scale	$H = 650\,\text{m}$
Coriolis parameter	$f_0 = 10^{-4}\,\text{s}^{-1}$
β parameter	$\beta = 2 \times 10^{-11}\,(\text{ms})^{-1}$
Vortex radius	$R = 100\,\text{km}$
Peak vorticity	$\omega_0 = 2.5 \times 10^{-5}\,\text{s}^{-1}$
Wind magnitude	$V_w = 20\,\text{m}\,\text{s}^{-1}$
Drag coefficient	$C_D = 0.0025$

Table 1. Fixed flow parameters in all simulations.

function ψ as

$$u = \frac{\partial \psi}{\partial y}, \quad v = -\frac{\partial \psi}{\partial x}. \tag{3.2a,b}$$

The relative vorticity is the 2-D Laplacian of the stream function:

$$\omega = -\nabla^2 \psi. \tag{3.3}$$

Table 1 shows the parameters that are kept constant in all simulations. The flow domain is a square, closed box with lateral walls at $-L \leq x, y \leq L$. The fluid depth is constant, and there is no bottom friction. Some simulations are performed on the f-plane, in which the flow dynamics are equivalent to the purely 2-D case, while some others are performed on the β plane. The simulations are initialised with an intense isolated vortex (2.3) with peak vorticity $\omega_0 = 0.25 f_0$ and radial scale $R = 100\,\text{km}$. Note that we consider a rather strong vortex with maximum velocities of approximately $u_{max} \sim 1\,\text{m}\,\text{s}^{-1}$. The vortex initial position is at the origin (0, 0), so the structure is sufficiently far away from the walls ($R/L < 1$) at all times. We use no-slip conditions (by setting a small viscous parameter) to confine the wall effects within a thin boundary layer that does not influence the vortex.

The Ekman pumping w may be either w_d (1.2), w_a (1.3) or the combination $w_d + w_a$, as outlined in table 2. The wind stress is parametrised with the atmosphere-ocean relative velocity (1.4) using a constant wind with magnitude V_w in a fixed, arbitrary direction θ with respect to the positive x-direction:

$$\boldsymbol{U} = V_w(\cos\theta, \sin\theta), \quad -\pi \leq \theta \leq \pi. \tag{3.4}$$

For all f-plane simulations, we use the 'northerly' wind $\theta = -\pi/2$, but we also examine other directions in the β-plane simulations. To simulate strong atmospheric fronts, we focus on intense winds of $V_w = 20\,\text{ms}^{-1}$, for which $C_D = 2.5 \times 10^{-3}$ (e.g. García-Nava, Ocampo-Torres & Hwang 2012). The duration of the simulations is 30 days to appreciate significant changes in the vortex strength and position.

The numerical model is a finite differences code used in previous works to simulate experimental rotating flows over topography (Zavala Sansón & van Heijst 2014) and turbulent wind-driven flows (Zavala Sansón 2022). Further details can be consulted in those studies. The nonlinear terms are discretised in a rectangular grid and treated with an Arakawa scheme to avoid the spurious production of energy or enstrophy in the inviscid limit. Time advancement is performed with an explicit, third-order Runge–Kutta method. In all cases shown below, there are 513×513 grid points ($\mathrm{d}x = \mathrm{d}y \approx 2.3\,\text{km}$) and the time step is $\mathrm{d}t = 3600\,\text{s}$. Several preliminary runs were performed with a lower resolution of 257×257 points, and the results were essentially the same.

Subsection	Number #	Plane	Vortex	Pumping	Wind provenance (θ)
3.2 and 3.3	A1	f	Anticyclone	w_d	N $(-\pi/2)$
Vortex decay and drift	A2	f	Anticyclone	w_a	N $(-\pi/2)$
	A3	f	Anticyclone	$w_d + w_a$	N $(-\pi/2)$
	A4	f	Anticyclone	w_{lin}	N $(-\pi/2)$
	C1	f	Cyclone	w_d	N $(-\pi/2)$
	C2	f	Cyclone	w_a	N $(-\pi/2)$
	C3	f	Cyclone	$w_d + w_a$	N $(-\pi/2)$
	C4	f	Cyclone	w_{lin}	N $(-\pi/2)$
3.4	A0	β	Anticyclone	—	—
Vortex β-drift	AN	β	Anticyclone	w_a	N $(-\pi/2)$
	AS	β	Anticyclone	w_a	S $(\pi/2)$
	AE	β	Anticyclone	w_a	E (π)
	AW	β	Anticyclone	w_a	W (0)
	C0	β	Cyclone	—	—
	CN	β	Cyclone	w_a	N $(-\pi/2)$
	CS	β	Cyclone	w_a	S $(\pi/2)$
	CE	β	Cyclone	w_a	E (π)
	CW	β	Cyclone	w_a	W (0)

Table 2. Outline of the simulations. The pumping term in experiments A4 and C4 is given by (2.15).

3.2. *Evolution of vortices*

To illustrate the effects of the Ekman pumping terms separately, we consider an anticyclonic vortex subject to large-scale northerly wind, $\theta = -\pi/2$ in (3.4), equivalent to (2.2*a*,*b*) (experiments A1, A2 and A3 in table 2). Although these simulations are performed on the f-plane, we will refer to the uniform wind as 'northerly' because it is directed downward in the planar plots, and for a better comparison with the β-plane simulations presented in § 3.4.

Figure 5 presents the vorticity fields at the initial time and 30 days after in the three experiments. When the Ekman pumping is only w_d (figure 5*a*), the vorticity field decays (as appreciated from the colour scale); however, the vortex stays at its initial position and does not change its shape appreciably. When the pumping is only w_a (figure 5*b*), the vorticity field does not change appreciably but the vortex drifts westward with a slight southward component. Recall that the vortex drift takes place in the direction of the Ekman transport (westward, for the northerly wind). When the two Ekman pumping components are considered (figure 5*c*), we observe that the vortex experiences both effects: it decays and moves westward.

The vertical velocity fields induced by the pumping terms are shown in figure 6. For w_d (figure 6*a*), we observe the characteristic upwelling at the central part (flanked by two elongated downwelling regions), which is weakened after 30 d. The up-and-downwelling pattern generated by the vertical velocity w_a (figure 6*b*) drifts westward with the vortex and does not decay in time. Note that the magnitude of w_a is greater than that of w_d at the initial and final times. When the two effects are considered (figure 6*c*), we observe an upwelling/downwelling pattern that differs from the current-induced upwelling w_d (in figure 6*a*) and is more similar to the w_a field (figure 6*b*). Again, the structure weakens in time and drifts to the west.

To compare the difference between cyclones and anticyclones, figure 7 presents the vorticity profiles along the x-direction at times 0 and 30 d. In figure 7(*a*), we observe that

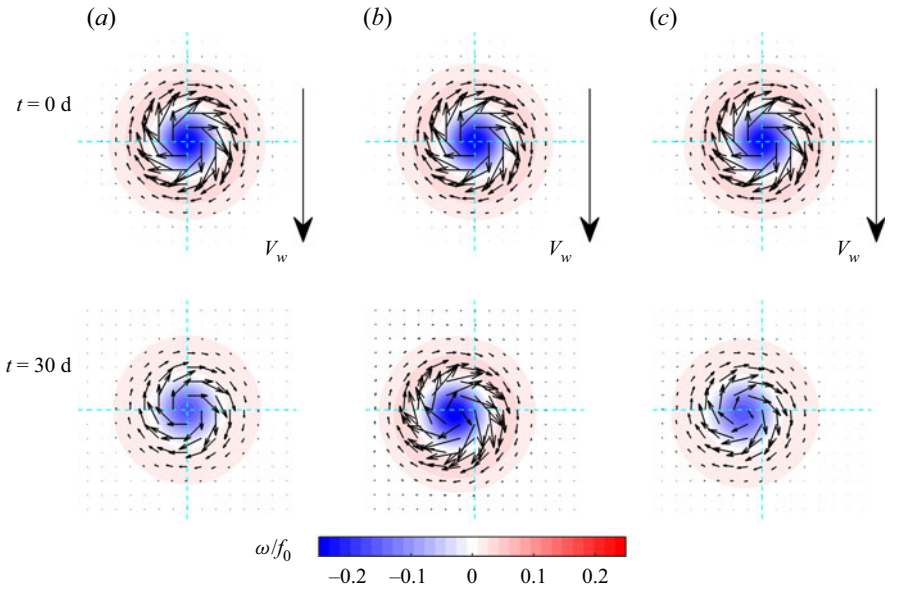

Figure 5. Numerically calculated relative vorticity surfaces in: (*a*) experiment A1 using only w_d; (*b*) experiment A2 using w_a; (*c*) experiment A3 using $w_d + w_a$ for (top) the initial time and (bottom) 30 days. The flow parameters are shown in table 1. The vertical and horizontal dashed lines are drawn to identify the initial vortex position and displacement.

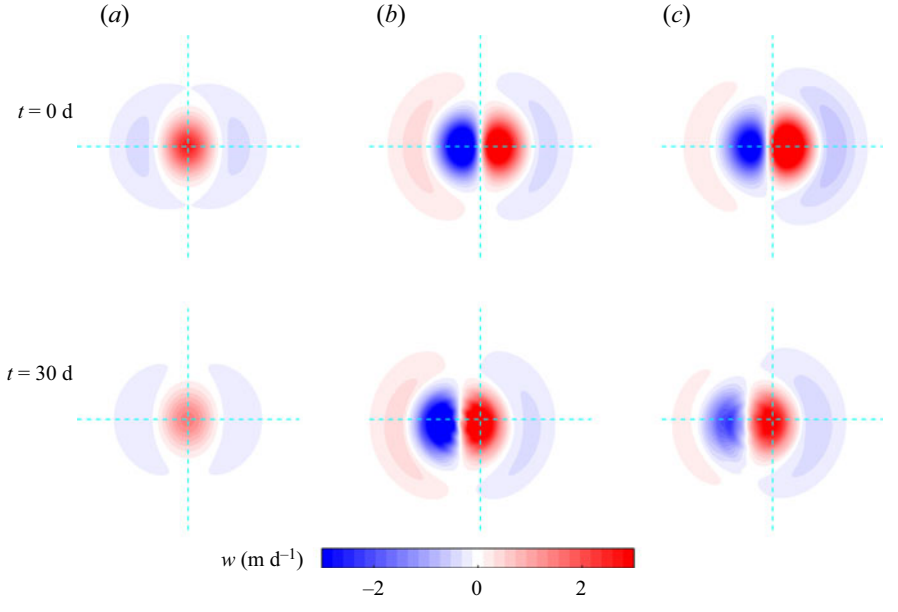

Figure 6. Ekman pumping surfaces in experiments A1, A2 and A3 shown in figure 5: (*a*) w_d; (*b*) w_a; (*c*) $w_d + w_a$.

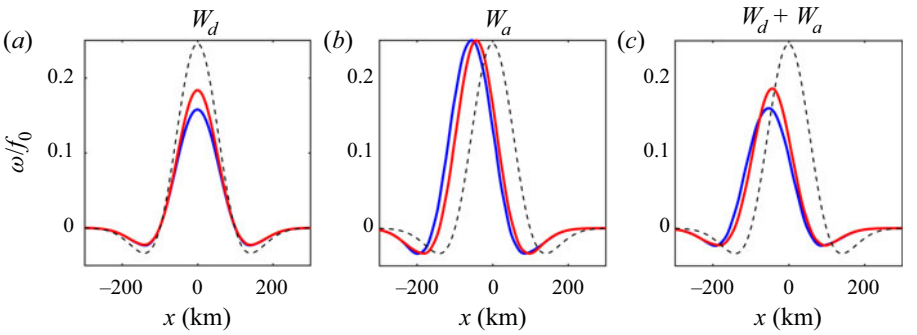

Figure 7. Vorticity x-profiles (passing over the vortex centre) for cyclones (red) and anticyclones (blue) at $t = 30$ d in experiments: (*a*) A1, C1; (*b*) A2, C2; (*c*) A3, C3. The anticyclone profiles are multiplied by -1 to facilitate the comparison. The profiles at $t = 0$ d are shown with dashed curves.

the anticyclone decays more than the cyclone due to w_d; figure 7(*b*) shows that w_a promotes the westward drift of both vortices while the peak vorticity remains constant; finally, figure 7(*c*) shows the combined effects in the two vortices (decay and displacement). In what follows, we evaluate these effects quantitatively and test the theoretical predictions derived in the previous section.

3.3. *Decay of cyclones and anticyclones*

Let us consider the influence of the Ekman pumping terms on the vortex strength. Figure 8(*a*) presents the time evolution of the normalised peak vorticity $\omega_c(t)$ in four simulations: two of them for an anticyclone using w_d, w_a (A1 and A2) and the corresponding cases for a cyclone (C1 and C2). The curves show that the peak vorticity in the anticyclone decays faster than in the cyclone when the only pumping term is w_d. The analytical expression (2.14) for the nonlinear decay is also shown for both vortices (magenta curves), which agree very well with the numerical results. The decay time scale (2.13) is $T \approx 84$ days. The figure also shows the exponential decay given by (2.17) (dashed line), which lies between the cyclone and anticyclone curves. Regarding the w_a effects, the peak vorticity remains constant because w_a is zero at the centre of a circular vortex, as can be observed in the vorticity profiles in figure 2(*c*,*d*). This is also evident by noticing from the w_a definition (1.3) that $\partial\omega/\partial x = \partial\omega/\partial y = 0$ at the centre of a circular structure. However, w_a plays a role in the kinetic energy budget, as discussed below.

In figure 8(*b*), we compare the peak vorticity decay of the cyclone and the anticyclone in simulations using the two Ekman terms (experiments A3 and C3). The curves are virtually the same as the previous simulations with w_d because the contribution of w_a to this parameter is nearly zero. We also plotted the exponential decay from simulations using w_{lin} (experiments A4 and C4), which collapse into one single curve (black line). Overall, the results prove that the peak vorticity value at the eddy's centre decays faster in the anticyclone than in the cyclone and that the mechanism is the w_d pumping term.

Now we examine the evolution of the kinetic energy integrated over a circular area S surrounding the vortex

$$E = \frac{1}{2}\int_S (u^2 + v^2)\,\mathrm{d}S. \tag{3.5}$$

We use $S = \pi R_s^2$ with $R_s = 3R$. Figure 9 shows the energy curves for the same experiments shown in previous plots. In figure 9(*a*), it is found again that, when using only w_d, the

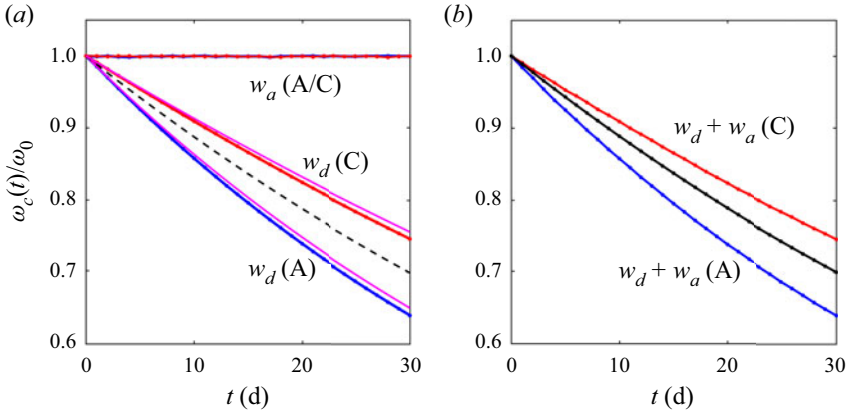

Figure 8. Temporal evolution of the peak vorticity in anticyclonic (blue) and cyclonic (red) vortices subject to different pumping effects. (*a*) Experiments A1, C1 (using w_d) and A2, C2 (using w_a). The analytical nonlinear decay (2.14) for cases A1, C1 is indicated with solid magenta lines. The linear decay (2.17) is represented by the dashed curve. (*b*) Simulations of the same vortices but now using $w_d + w_a$ (experiments A3, C3). The black curve corresponds to simulations with linear decay A4, C4.

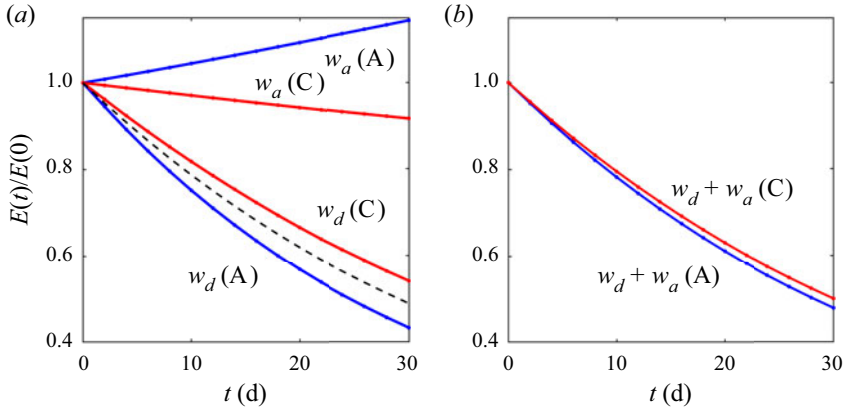

Figure 9. Temporal evolution of the vortex kinetic energy defined in (3.5) for cyclones (red) and anticyclones (blue). (*a*) Experiments A1, C1 (using w_d) and A2, C2 (using w_a). The standard decay (3.6) is represented by the dashed curve. (*b*) Simulations of the same vortices but now using $w_d + w_a$ (experiments A3, C3).

kinetic energy in the anticyclone decays faster than in the cyclone. Between the two decreasing curves, we plotted the expected energy curve corresponding to the exponential decay:

$$E(t) = E(0)\exp(-2t/T). \tag{3.6}$$

The e-folding time $T/2$ is due to the quadratic form of the kinetic energy (see e.g. Zavala Sansón *et al.* 2001; Renault *et al.* 2016). What is different now is the effect of w_a: the energy increases in the anticyclone and decays in the cyclone. These changes due to w_a are smaller than the decay due to w_d, but they are evident. The cause for these behaviours is the net downwelling flow that results from the azimuthal integration of the w_a dipolar field (described in figure 3*c*,*d*). Indeed, the average downward velocity $\bar{w}_a$ is faster in the anticyclone, so its intensification (approximately 12 % in kinetic energy after 30 days) is greater than the weakening of the cyclone (approximately 9 %).

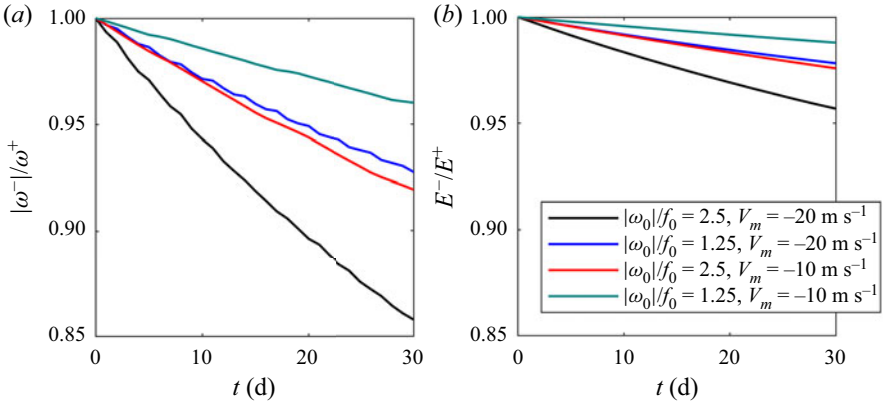

Figure 10. Temporal evolution of (a) the peak vorticity ratio $|\omega^-|/\omega^+$ between anticyclones and cyclones for different vortex amplitudes ω_0 and wind speeds V_m, and (b) the corresponding kinetic energy ratio E^-/E^+.

Figure 9(b) presents the kinetic energy decay of the cyclone and anticyclone in the simulations using the two Ekman terms. The curves almost collapse, with the anticyclonic decay being slightly faster. For the anticyclone, this means that the energy decay due to w_d is compensated by the energy increase due to w_a. For the cyclone, both effects produce energy decay but with a smaller magnitude, so the final curve is almost identical to that of the anticyclone.

How is the anticyclone/cyclone asymmetric decay in terms of the wind speed and vortex strength? To explore this question, we performed new experiments using $w_d + w_a$ and measured the time evolution of the anticyclone/cyclone peak vorticity and the kinetic energy ratios, defined as $|\omega^-|/\omega^+$ and E^-/E^+, respectively. The results are presented in figure 10(a,b) for different combinations of the initial peak vorticity ω_0 and wind speed V_m. At $t = 0$, the curves start at 1 and, since anticyclones decay faster, the curves decay in time. The resulting ratios for the vortices presented in figures 8(b) and 9(b) are plotted with black lines. Both ratios decay less for weaker vortices and wind speeds (see e.g. the green curves), indicating a more symmetrical behaviour of cyclones and anticyclones.

3.4. *Vortex drift*

We showed in figures 5–7 that the Ekman pumping w_a induces the vortex drift (2.20) to the right of the wind direction. Figure 11 presents the kinetic energy field and the numerically calculated trajectory of anticyclone A2 and cyclone C2 (that is, under the influence of w_a alone) at day 30. The westward displacements are 56.3 km for the anticyclone and 42.2 km for the cyclone. These values agree with the displacements calculated with (2.20), which gives $\Delta x = 59.6$ and 35.8 km, respectively. Note also that the numerical trajectory is not purely westward, but there is a small southward shift (approximately 9 km in both simulations). Overall, the experiments confirm that the anticyclone drifts to the right of the wind at the predicted speed and faster than the cyclone. The kinetic energy fields demonstrate that the anticyclone is reinforced compared with the cyclone, as shown in figure 9(a).

Now we will examine the vortex trajectory on the β-plane. Recall that nonlinear barotropic anticyclones (cyclones) on a β-plane drift southwestward (northwestward) (Adem 1956). In particular, intense shielded vortices as those defined by (2.3) follow a trochoid trajectory with a strong meridional component (Zavala Sansón, van Heijst &

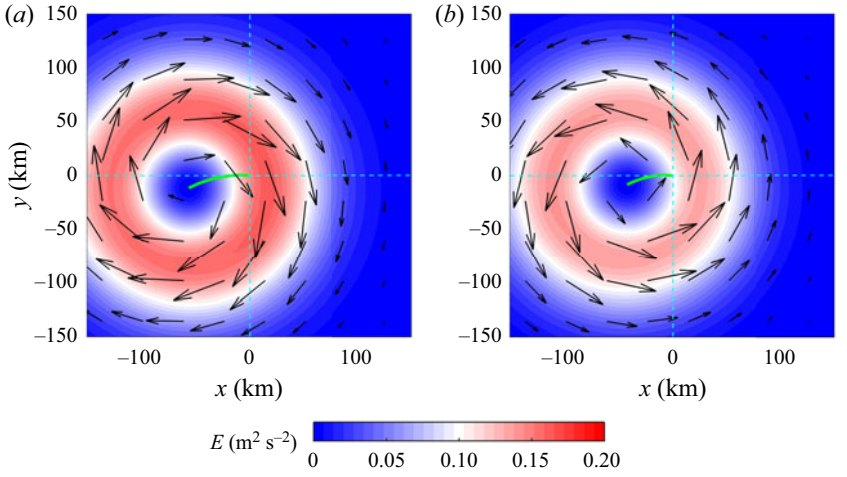

Figure 11. Kinetic energy surfaces and velocity vectors in simulations using w_a: (*a*) anticyclone A2; (*b*) cyclone C2. The vortex displacement is shown with green curves. The maximum velocity is 0.55 m s^{-1}. Vertical and horizontal dashed lines are drawn to identify the vortex initial position at the origin.

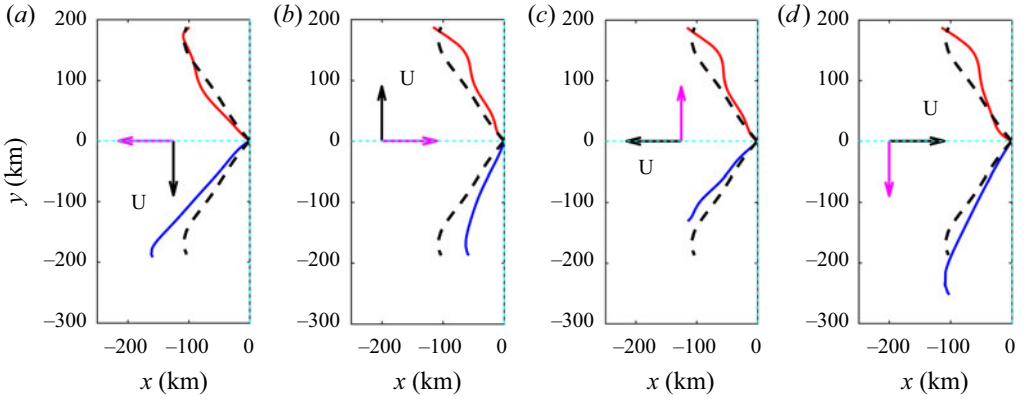

Figure 12. Vortex trajectories calculated in β-plane simulations with different wind provenance: (*a*) northerly wind (simulations AN, CN); (*b*) southerly (AS, CS); (*c*) easterly (AE, CE); (*d*) westerly (AW, CW). Cyclone (anticyclone) trajectories are denoted with red (blue) curves. In all panels, the trajectories in the absence of wind are shown with dashed lines (experiments A0, C0). In each panel, the black arrow indicates the wind direction and the magenta arrow the direction of the Ekman transport.

Doorschot 1999; Flór & Eames 2002). Then we may ask, what is the effect of the Ekman term w_a on the vortex drift? To answer this question, we performed several simulations for cyclones and anticyclones (see table 2). Note that we only consider w_a because it is the pumping term responsible for the vortex drift, so we omit the decaying effects associated with w_d. It must be taken into account that now the wind direction is of fundamental importance. Thus, we analysed the vortex trajectories in five simulations: a reference experiment with no Ekman terms (cases A0 and C0, dashed lines), and four simulations using w_a and having the wind provenance from the cardinal directions (figure 12).

Let us focus first on the anticyclones (drifting southwestward – blue curves). In all cases, we can observe that the trajectory is deflected from the reference run according to the wind direction. For instance, for the northerly wind (figure 12*a*), the vortex trajectory

is deflected to the west. In contrast, for southerly wind (figure 12*b*), the Ekman drift is eastward, and the trajectory is deflected more to the south. Note that the β-drift may be arrested (figure 12*c*) or augmented (figure 12*d*). For cyclones (drifting northwestward), we observe that the trajectories are also deflected from the reference experiment depending on the wind direction. An exception is the case shown in figure 12(*d*) (westerly wind). In general, the nonlinear character of the problem rules out the possibility of explaining the details of the trajectories because of the complex convolution of the vorticity contours as the eddies drift, and the radiation of Rossby waves (McWilliams & Flierl 1979; Flór & Eames 2002).

3.5. *Extended vorticity equation*

Let us examine additional simulations based on the vorticity equation that retains the absolute vorticity in the forcing term

$$\frac{\partial \omega}{\partial t} + J\left(\omega + \beta y, \psi\right) = \frac{(f+\omega)}{H} w_s. \tag{3.7}$$

Although we show in Appendix A that the β and ω terms on the right-hand side can be neglected because of magnitude grounds (so the dominant forcing term is $f_0 w/H$), here we explore the consequences of keeping them.

When using the Ekman pumping terms w_d and w_a in (3.7), the absolute vorticity $f+\omega$ cancels out, such that:

$$\frac{(f+\omega)}{H}(w_d + w_a) = \frac{1}{H\rho_0}\boldsymbol{\nabla}\times\boldsymbol{\tau} + \frac{1}{H\rho_0(f+\omega)}\left(\tau^x\frac{\partial\omega}{\partial y} - \tau^y\frac{\partial\omega}{\partial x}\right). \tag{3.8}$$

Thus, the forcing term $(f+\omega)w_d/H$ becomes identical to the linear case $f_0 w_{lin}/H$, with w_{lin} given by (2.15). A notorious consequence is that cyclones and anticyclones now decay at the same rate: w_d no longer distinguishes the vortex polarity. In contrast, the effects due to w_a remain nonlinear, so its influence on vortices is similar as before: w_a weakens (intensifies) cyclones (anticyclones) and promotes their drift to the right of the wind direction.

To show these assertions, we reproduced all the simulations in table 2 but now using (3.7). In general, the results are qualitatively similar, though there are important differences to mention. We focus on the global energy evolution. Figure 13 presents the vortex energy for the same cases shown in figure 9. First, note that in figure 13(*a*), when using w_d, the cyclone and the anticyclone decay in the same fashion: the curves are overlapped and are given by (3.6). Second, when using w_a, the energy evolves in a similar way as in figure 9: the anticyclone is intensified and the cyclone weakened. Interestingly, when using $w_d + w_a$ (figure 13*b*), the net energy decay of the cyclone is notoriously faster than that of the anticyclone. Of course, the difference is due to w_a, since w_d produces the same decay.

4. Summary and discussion

We discussed the effects of the Ekman pumping terms w_d (1.2) and w_a (1.3) due to a uniform, uni-directional intense wind blowing over nonlinear cyclones and anticyclones governed by the vorticity equation (2.1). The surface wind stress is parametrised with the relative air-sea velocity, so there are current-feedback effects. It is well known that the vertical velocity w_d tends to drain the vortex kinetic energy because it has the opposite sign of the vortex core (Dewar & Flierl 1987). The role of w_a is more controversial, as its magnitude is usually similar to or even greater than that of w_d, but the net up

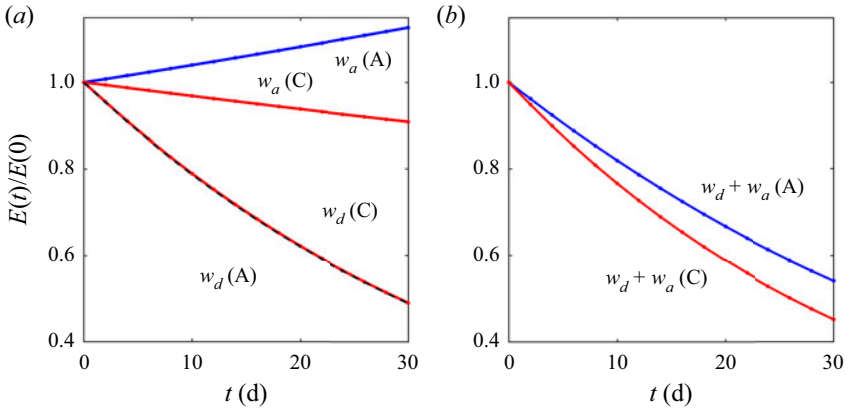

Figure 13. Temporal evolution of the vortex kinetic energy of cyclones (red) and anticyclones (blue) in experiments using the extended vorticity equation (3.7). Compare with the curves shown in figure 9: (*a*) A1, C1 (using w_d) and A2, C2 (using w_a). A1, C1 decay at the same rate (the curves are overlapped); (*b*) A3, C3 ($w_d + w_a$).

or downwelling flow is very weak due to its dipolar spatial distribution (see figure 3). However, its magnitude contributes to the spatial distribution of vertical transport, a fundamental issue for nutrient delivery that influences plankton dynamics (Estrada-Allis *et al.* 2019; Chen *et al.* 2020). The main analytical and numerical results are the following.

(i) The top drag mechanism associated with the Ekman pumping w_d makes anticyclones decay faster than cyclones. This difference is found when considering the absolute vorticity in the denominator of the w_d definition (1.2), which leads to the nonlinear equation for the peak vorticity (2.12). From the analytical solution, we found the decay time scale T defined in (2.13), which is identical to the scale derived by Gaube *et al.* (2015) under different assumptions (they considered a randomly directed wind). A differential decay between cyclones and anticyclones also occurs when considering nonlinear Ekman effects generated at the lower Ekman layer, but in that case, cyclones decay faster than anticyclones (Zavala Sansón *et al.* (2001) and Zavala Sansón (2001), see § 1).

(ii) The net pumping $\bar{w}_a$ is weakly negative for both types of vortices (figure 3*c*,*d*) and, consequently, anticyclones (cyclones) are intensified (weakened) (figure 11). Such a downward velocity has not been sufficiently discussed in previous studies, probably because the mean values tend to be small (of the order of $0.1\,\mathrm{m\,d^{-1}}$). Furthermore, the damping effect due to w_d is more persistent, thus obscuring the integrated w_a effects. The production or destruction of barotropic kinetic energy through this mechanism may have consequences for the vortex stability. For instance, the intensification of anticyclones (2.3) may lead to steeper vorticity profiles that are more prone to barotropic (Orlandi & Carnevale 1999) or centrifugal (Kloosterziel & van Heijst 1991) instabilities.

(iii) Another effect produced by the pumping term w_a is the vortex drift at the speed and direction of the Ekman transport. When the wind blows, the mean horizontal motion in the Ekman layer tries to tilt the axis of the geostrophic vortex. However, in the constant-depth barotropic model, the fluid columns remain vertical (due to the rotational constraint), and the vortex moves with speed equal to the Ekman drift, as predicted by Stern (1965). In our f-plane simulations, we also found a small drift in the wind direction (figure 11). The origin of this additional displacement

is unknown, but it could be related to an Ekman transport component along the wind direction due to the flow curvature, as discussed by Wenegrat & Thomas (2017). However, that study only considered a constant wind stress, so there are no current-induced pumping effects. A possible line of research would be to calculate curvature effects but now using the relative-velocity parametrisation for circular vortices. Furthermore, we examined the modification of vortex trajectories in β-plane simulations due to the additional drift induced by w_a.

(iv) When the two pumping terms are considered together, the decrease of the net kinetic energy becomes similar in cyclones and anticyclones (figure 9). The slight asymmetry tends to disappear for weaker vortices and/or slower winds.

The relative importance of the Ekman terms depends on the problem under study, and a proper evaluation of which one is more important might require a comparison of their magnitude or spatial structure. Mahadevan *et al.* (2008) proposed that the ratio of the pumping magnitudes scales as $Ro(u_a/u_o)$, with Ro the Rossby number, and u_a, u_o the velocity scales of the wind and the ocean, respectively. Such an expression does not distinguish cyclones from anticyclones. A similar scaling was proposed by Chen *et al.* (2020) as $-Ro(u_a/2u_o)/(1+Ro)$, whose denominator is able to distinguish the vortex polarity. We proposed scaling (2.22), which coincides in that $|w_a/w_d|$ depends linearly on the wind speed but explicitly depends only on $(1+Ro)^{-1}$ (figure 4). In addition, we estimated another scaling that considers the spatial structure (2.24). This expression indicates that $|\bar{w}_a/\bar{w}_d| < 1$, so the current-induced term is more relevant. A similar conclusion led McGillicuddy *et al.* (2008) to consider only w_d and neglect w_a for explaining the persistent vertical transport of nutrients in oceanic eddies.

The two-dimensional approach used here offers the advantage of studying w_d and w_a separately in numerical simulations that solve the vorticity equation (2.1). Such a procedure is difficult to achieve when using more realistic three-dimensional models, even in idealised simulations. For instance, Chen *et al.* (2020) and Wilder *et al.* (2022) performed baroclinic simulations of idealised anticyclonic vortices using the wind stress parametrisation (1.4). However, the effects of a persistent wind in a single direction were filtered out because the wind direction was rotated uniformly in time (one full rotation every 64 h) to avoid vortex distortions, boundary problems or bias of the sea level slope in one particular direction. Chen *et al.* (2020) also performed simulations with realistic wind forcing. Under these conditions, some Ekman effects may be reduced or inhibited, such as the vortex drift due to w_a. It remains to be seen whether the Ekman effects observed in the barotropic approach are sufficiently important in baroclinic models or more realistic wind conditions.

We also explored the form of the Ekman term in the dynamical equation. When using the vorticity equation (3.7), which includes the absolute vorticity in the forcing term, some of the previous results hold and some others change sensibly. Essentially, the vortex decay due to w_d no longer distinguishes cyclones from anticyclones because the absolute vorticity cancels with the denominator of w_d. Nevertheless, the cyclone/anticyclone asymmetry still holds but now only due to w_a, which generates similar effects to those described in items (ii) and (iii). When considering the two Ekman velocities together, the cyclone clearly decays faster (figure 13). It must be noted that the observed differences between simulations using (2.1) or (3.7) are not caused by the addition of a new small term, but to the fact that the analytical form of the Ekman term associated with w_d is modified. This issue requires further analysis in future works.

Finally, we point out the relevance of discerning Ekman effects in cyclones and anticyclones for a continuously forced turbulent fluid. Indeed, the asymmetric decay of

these vortices might lead to positive or negative skewness of relative vorticity fields. Future lines of research are the consequences for the two-dimensional turbulent cascades and the Ekman effects in other oceanic structures, such as dipolar vortices.

Acknowledgements. The authors gratefully acknowledge comments and helpful criticisms from the anonymous reviewers. I.G. and J.S. acknowledge financial support from CONACYT project FORDECYT-PRONACES 1327709/2020.

Declaration of interests. The authors report no conflict of interest.

Author ORCIDs.
L. Zavala Sansón https://orcid.org/0000-0002-0419-5445.

Appendix A

Consider a homogeneous, quasi-two-dimensional flow with a rigid-lid on a β-plane. The direct vertical integration of the vorticity equation over the fluid depth H yields

$$\frac{\partial \omega}{\partial t} + \boldsymbol{u} \cdot \nabla \omega + \beta v = \frac{(f_0 + \beta y + \omega)}{H} w_s, \tag{A1}$$

where the right-hand side is the stretching term produced by the Ekman pumping w_s. However, $(\beta y + \omega) w_s$ at the forcing term is usually neglected because of the smallness of the Ekman velocity, even for strong winds.

To verify this assertion, we can estimate the approximate size of all terms in (A1) using the typical velocity U_o and radial vortex scale L, which gives the following set of nondimensional numbers:

$$\epsilon = \frac{U_o}{f_0 L}, \quad \hat{\beta} = \frac{\beta L}{f_0}, \quad \widehat{W_1} = \frac{WL}{U_o H}, \quad \widehat{W_2} = \widehat{W_1}\hat{\beta}, \quad \widehat{W_3} = \widehat{W_1}\epsilon, \tag{A2a–e}$$

where $W \sim \rho_a C_D U_w^2$ is the vertical velocity scale based on the stress parametrisation (1.4) with the wind speed U_w, and assuming $U_w >> U_o$. The numbers $\widehat{W_1}$, $\widehat{W_2}$ and $\widehat{W_3}$ correspond to the Ekman terms. Evidently, for $\epsilon, \hat{\beta}, \widehat{W_1} < 1$, we get $\widehat{W_2}, \widehat{W_3} << 1$, so these two terms can be neglected. For instance, using the values in the manuscript ($U_o \sim 0.5\,\mathrm{m\,s^{-1}}$, $U_w \sim 20\,\mathrm{m\,s^{-1}}$, $W \sim 7 \times 10^{-5}\,\mathrm{m\,s^{-1}}$, $L \sim 100\,\mathrm{km}$, $H \sim 650\,\mathrm{m}$) gives

$$\epsilon \sim 0.05, \quad \hat{\beta} \sim 0.02, \quad \widehat{W_1} \sim 0.04, \quad \widehat{W_2} \sim 1.5 \times 10^{-4}, \quad \widehat{W_3} \sim 3.7 \times 10^{-3}. \tag{A3a–e}$$

Thus, the lasts two terms in (A1) are much smaller, so they are usually dropped in oceanic models.

What happens if the $O(\hat{W}_2, \hat{W}_3)$ terms are retained? For instance, when deriving the nonlinear pumping velocity w_s (1.1), Stern (1965) maintained the $O(\hat{W}_2)$ β term:

$$\frac{\partial \omega}{\partial t} + \boldsymbol{u} \cdot \nabla \omega + \beta v = \frac{f}{H} w_s \tag{A4}$$

[see his (17)]. At the end of § 3, we briefly discuss numerical simulations that include both the β and the ω term.

References

Adem, J. 1956 A series solution for the barotropic vorticity equation and its application in the study of atmospheric vortices. *Tellus* **8** (3), 364–372.

AMADOR, J.A. 2008 The intra-Americas sea low-level jet: overview and future research. *Ann. N.Y. Acad. Sci.* **1146** (1), 153–188.

CARTON, X.J & MCWILLIAMS, J.C. 1989 Barotropic and baroclinic instabilities of axisymmetric vortices in a quasigeostrophic model. Elsevier Oceanogr. Series, vol. 50, pp. 225–244. Elsevier.

CHELTON, D.B., SCHLAX, M.G. & SAMELSON, R.M. 2011 Global observations of nonlinear mesoscale eddies. *Prog. Oceanogr.* **91** (2), 167–216.

CHEN, K., GAUBE, P. & PALLÀS-SANZ, E. 2020 On the vertical velocity and nutrient delivery in warm core rings. *J. Phys. Oceanogr.* **50** (6), 1557–1582.

DAMIEN, P., SHEINBAUM, J., PASQUERON DE FOMMERVAULT, O., JOUANNO, J., LINACRE, L. & DUTEIL, O. 2021 Do Loop Current eddies stimulate productivity in the Gulf of Mexico? *Biogeosciences* **18** (14), 4281–4303.

DEWAR, W.K. & FLIERL, G.R. 1987 Some effects of the wind on rings. *J. Phys Oceanogr.* **17** (10), 1653–1667.

DING, M., LIN, P., LIU, H., HU, A. & LIU, C. 2020 Lagrangian eddy kinetic energy of ocean mesoscale eddies and its application to the Northwestern Pacific. *Sci. Rep.* **10**, 12791.

ESTRADA-ALLIS, S.N., BARCELÓ-LLULL, B., PALLÀS-SANZ, E., RODRÍGUEZ-SANTANA, A., SOUZA, J.M.A.C., MASON, E., MCWILLIAMS, J.C. & SANGRÀ, P. 2019 Vertical velocity dynamics and mixing in an anticyclone near the Canary Islands. *J. Phys. Oceanogr.* **49** (2), 431–451.

FLÓR, J.-B. & EAMES, I. 2002 Dynamics of monopolar vortices on a topographic beta-plane. *J. Fluid Mech.* **456**, 353–376.

GARCÍA-MARTÍNEZ, I.M. & BOLLASINA, M.A. 2020 Sub-monthly evolution of the Caribbean Low-Level Jet and its relationship with regional precipitation and atmospheric circulation. *Clim. Dyn.* **54** (9), 4423–4440.

GARCÍA-NAVA, H., OCAMPO-TORRES, F.J. & HWANG, P.A. 2012 On the parameterization of the drag coefficient in mixed seas. *Scientia Marina* **76** (S1), 177–186.

GAUBE, P., CHELTON, D.B., SAMELSON, R.M., SCHLAX, M.G. & O'NEILL, L.W. 2015 Satellite observations of mesoscale eddy-induced Ekman pumping. *J. Phys. Oceanogr.* **45** (1), 104–132.

VAN HEIJST, G.J.F. & CLERCX, H.J.H. 2009 Laboratory modeling of geophysical vortices. *Annu. Rev. Fluid Mech.* **41**, 143–164.

HELLERMAN, S. 1967 An updated estimate of the wind stress on the world ocean. *Mon. Weath. Rev.* **95** (9), 607–626.

JOUANNO, J., SHEINBAUM, J., BARNIER, B., MOLINES, J.M. & CANDELA, J. 2012 Seasonal and interannual modulation of the eddy kinetic energy in the Caribbean Sea. *J. Phys. Oceanogr.* **42** (11), 2041–2055.

KLEIN, P., LAPEYRE, G., SIEGELMAN, L., QIU, B., FU, L.L., TORRES, H., SU, Z., MENEMENLIS, D. & LE GENTIL, S. 2019 Ocean-scale interactions from space. *Earth Space Sci.* **6** (5), 795–817.

KLOOSTERZIEL, R.C. & VAN HEIJST, G.J.F. 1991 An experimental study of unstable barotropic vortices in a rotating fluid. *J. Fluid Mech.* **223**, 1–24.

KLOOSTERZIEL, R.C. & VAN HEIJST, G.J.F. 1992 The evolution of stable barotropic vortices in a rotating free-surface fluid. *J. Fluid Mech.* **239**, 607–629.

MAHADEVAN, A., THOMAS, L.N. & TANDON, A. 2008 Comment on "Eddy/wind interactions stimulate extraordinary mid-ocean plankton blooms". *Science* **320** (5875), 448–448.

MAHDINIA, M., HASSANZADEH, P., MARCUS, P.S. & JIANG, C.H. 2017 Stability of three-dimensional Gaussian vortices in an unbounded, rotating, vertically stratified, Boussinesq flow: linear analysis. *J. Fluid Mech.* **824**, 97–134.

MCGILLICUDDY, D.J., LEDWELL, J.R. & ANDERSON, L.A. 2008 Response to comment on "Eddy/wind interactions stimulate extraordinary mid-ocean plankton blooms". *Science* (5875), 448.

MCGILLICUDDY, D.J. JR., *et al.* 2007 Eddy/wind interactions stimulate extraordinary mid-ocean plankton blooms. *Science* **316** (5827), 1021–1026.

MCGILLICUDDY, D.J. JR. 2016 Mechanisms of physical-biological-biogeochemical interaction at the oceanic mesoscale. *Annu. Rev. Mar. Sci.* **8**, 125–159.

MCWILLIAMS, J.C. & FLIERL, G.R. 1979 On the evolution of isolated, nonlinear vortices. *J. Phys. Oceanogr.* **9** (6), 1155–1182.

MEUNIER, T., SHEINBAUM, J., PALLÀS-SANZ, E., TENREIRO, M., OCHOA, J., RUIZ-ANGULO, A., CARTON, X. & DE MAREZ, C. 2020 Heat content anomaly and decay of warm-core rings: the case of the Gulf of Mexico. *Geophys. Res. Lett.* **47** (3), e2019GL085600.

MKHININI, N., COIMBRA, A.L.S., STEGNER, A., ARSOUZE, T., TAUPIER-LETAGE, I. & BÉRANGER, K. 2014 Long-lived mesoscale eddies in the eastern Mediterranean Sea: analysis of 20 years of AVISO geostrophic velocities. *J. Geophys. Res.* **119** (12), 8603–8626.

ORLANDI, P. & CARNEVALE, G.F. 1999 Evolution of isolated vortices in a rotating fluid of finite depth. *J. Fluid Mech.* **381**, 239–269.

PACANOWSKI, R.C. 1987 Effect of equatorial currents on surface stress. *J. Phys. Oceanogr.* **17** (6), 833–838.

PEDLOSKY, J. 1987 *Geophysical Fluid Dynamics*. Springer.

RAI, S., HECHT, M., MALTRUD, M. & ALUIE, H. 2021 Scale of oceanic eddy killing by wind from global satellite observations. *Sci. Adv.* **7** (28), eabf4920.

RENAULT, L., MOLEMAKER, M.J., MCWILLIAMS, J.C., SHCHEPETKIN, A.F., LEMARIÉ, F., CHELTON, D., ILLIG, S. & HALL, A. 2016 Modulation of wind work by oceanic current interaction with the atmosphere. *J. Phys. Oceanogr.* **46** (6), 1685–1704.

ROMERO CENTENO, R. & ZAVALA HIDALGO, J. 2021 Meteorología. Atlas de línea base ambiental del Golfo de México (Tomo I), México: Consorcio de Investigación del Golfo de México.

STEGNER, A. & DRITSCHEL, D.G. 2000 A numerical investigation of the stability of isolated shallow water vortices. *J. Phys. Oceanogr.* **30** (10), 2562–2573.

STERN, M.E. 1965 Interaction of a uniform wind stress with a geostrophic vortex. *Deep Sea Res. Oceanogr. Abstr.* **12**, 355–367.

TENREIRO, M., CANDELA, J., PALLÀS SANZ, E., SHEINBAUM, J. & OCHOA, J. 2018 Near-surface and deep circulation coupling in the western Gulf of Mexico. *J. Phys. Oceanogr.* **48** (1), 145–161.

VALLIS, G.K. 2017 *Atmospheric and Oceanic Fluid Dynamics*. Cambridge University Press.

WENEGRAT, J.O. & THOMAS, L.N. 2017 Ekman transport in balanced currents with curvature. *J. Phys. Oceanogr.* **47** (5), 1189–1203.

WILDER, T., ZHAI, X., MUNDAY, D. & JOSHI, M. 2022 The response of a baroclinic anticyclonic eddy to relative wind stress forcing. *J. Phys. Oceanogr.* **52** (9), 2129–2142.

XU, C., ZHAI, X. & SHANG, X. 2016 Work done by atmospheric winds on mesoscale ocean eddies. *Geophys. Res. Lett.* **43** (23), 12–174.

ZAVALA SANSÓN, L. 2001 The asymmetric Ekman decay of cyclonic and anticyclonic vortices. *Eur. J. Mech.* B*/Fluids* **20** (4), 541–556.

ZAVALA SANSÓN, L. 2022 Effects of mesoscale turbulence on the wind-driven circulation in a closed basin with topography. *Geophys. Astrophys. Fluid Dyn.* **116** (3), 159–184.

ZAVALA SANSÓN, L. & VAN HEIJST, G.J.F. 2000 Nonlinear Ekman effects in rotating barotropic flows. *J. Fluid Mech.* **412**, 75–91.

ZAVALA SANSÓN, L. & VAN HEIJST, G.J.F. 2002 Ekman effects in a rotating flow over bottom topography. *J. Fluid Mech.* **471**, 239–255.

ZAVALA SANSÓN, L. & VAN HEIJST, G.J.F. 2014 Laboratory experiments on flows over bottom topography. In *Modeling Atmospheric and Oceanic Flows: Insights from Laboratory Experiments and Numerical Simulations* (ed. T. von Larcher & P.D. Williams). Wiley.

ZAVALA SANSÓN, L., VAN HEIJST, G.J.F. & BACKX, N.A. 2001 Ekman decay of a dipolar vortex in a rotating fluid. *Phys. Fluids* **13** (2), 440–451.

ZAVALA SANSÓN, L., VAN HEIJST, G.J.F. & DOORSCHOT, J.J.J. 1999 Reflection of barotropic vortices from a step-like topography. *Nuovo Cimento* C **22** (6), 909–930.

ZHANG, Z., QIU, B., TIAN, J., ZHAO, W. & HUANG, X. 2018 Latitude-dependent finescale turbulent shear generations in the Pacific tropical-extratropical upper ocean. *Nat. Commun.* **9**, 4086.